Oxygen Vacancies of Commercial V$_2$O$_5$ Induced by Mechanical Force to Enhance the Diffusion of Zinc Ions in Aqueous Zinc Battery

Danyang Zhao,[a] Qiancheng Zhu,*[b] Xiaohui Li,[a] Menghan Dun,[a] Yin Wang,[c] and Xintang Huang*[a]

Rechargeable aqueous batteries with Zn^{2+} as a media-ion are promising candidates for large-scale energy storage because of their intrinsic safety, low-cost and high energy-intensity. Vanadium based cathodic materials have gained significant attention in aqueous zinc-ion batteries (AZIBs) due to their high capacity and satisfactory cycle stability. However, more facile and efficient fabrication methods should be explored when considering future realistic application. Herein, commercial V$_2$O$_5$ cathodes with oxygen vacancies were fabricated through a simple mechanical ball milling method. The results suggest that mechanical force can directly induce the oxygen vacancies in commercial V$_2$O$_5$, which significantly enhance the diffusion of Zn ions. The oxygen vacancy–V$_2$O$_5$ (O$_v$–V$_2$O$_5$) shows much higher capacity than the pristine commercial V$_2$O$_5$ and the cyclic stability reached 2500 times. O$_v$–V$_2$O$_5$ cathode with a facile synthesis technology is a promising candidate for future high-performance, low-cost, safe, and environment-friendly Zn battery devices.

Introduction

Pursuing low-cost and safe batteries with high energy density is an eternal research target for largescale energy storage applications.[1] Li-ion batteries have been the dominating commercial power source for widely applied energy storage devices in decades due to its high output energy density and voltage.[2] Unfortunately, the disadvantages of scarce abundance with increasing cost of Li, unsafety and environmental hazard pose challenge for its large-scale application.[3] By contrast, rechargeable aqueous batteries using alkaline cations such as Li$^+$, Na$^+$, K$^+$, Mg^{2+}, Ca^{2+}, Al^{3+}, and Zn^{2+} as charge carriers show excellent safety, facile assembly and environmental benignity, which are promising alternatives for grid-scale electrochemical energy storage.

In particular, aqueous zinc-ion batteries (AZIBs) outperform the others owing to the properties of Zn anodes, including high abundance, nontoxicity, high capacity through a two-electron transfer (820 mAh g^{-1}) and appropriate redox potential (−0.76 V versus standard hydrogen electrode).[1d,2a,4] To enable high capacity, stability and rate capability for AZIBs, the desired cathode host should have a robust crystal architecture allowing fast and reversible Zn^{2+} intercalation.[5] Mn-based and V-based compounds are typical intercalation-type cathode materials in ZIBs for their high capacity (> 300 mAh g^{-1}).[6] However, pure manganese oxides and vanadium oxides show poor performance due to their compact crystal architecture, which is unbeneficial for the intercalation of Zn ions or protons. Thus, crystal architecture reform is necessary to further acquire promising performance, which includes the water molecules intercalation,[6c,7] polymer intercalation[8] and metal ions insertion,[5c,6d,9] etc. Specially, metal ions insertion is the most common method to remold crystal architecture. Recently, layered metal vanadates (A$_x$V$_m$O$_n$, A is metal cations) with open framework crystal structure have been applied to AZIBs,[3b,6d,9b,10] where metal cations embedded in the V$_m$O$_n$ layers act as strong pillars to provide expanded interlayer spacing for high-efficiency Zn^{2+} intercalation/deintercalation. Additionally, oxygen-deficient vanadium oxide fabricated by annealing in H$_2$ were also proved with higher performance than the ordinary vanadium oxide.[11] However, those materials fabrication method is always complicated and even multi-step synthesis processes are required, which enhances the cost of raw materials and synthesis technology. Thus, much simplified and effective fabrication method is in urgent need for future commercial application of AZIBs.

Mechanical ball milling method is a promising synthesis technology for future large-scale materials fabrication, which can even produce hundreds of tons materials in commercial technology.[12] However, acquiring high-performance Zn cathodic materials are still challenging by this method. Here, we

[a] D. Zhao, X. Li, M. Dun, Prof. X. Huang
Institute of Nanoscience and Nanotechnology
College of Physical Science and Technology
Central China Normal University
Wuhan 430079, China
E-mail: xthuang@mail.ccnu.edu.cn
[b] Dr. Q. Zhu
Hebei Key Laboratory of Optic-Electronic Information and Materials
National & Local Joint Engineering Laboratory
of New Energy Photoelectric Devices
College of Physics Science and Technology
Hebei University
Baoding 071002, China
E-mail: qcz@hbu.edu.cn
[c] Dr. Y. Wang
School of Physics and Electronic Engineering
Hubei University of Arts and Science
Xiangyang, 441053, China

found mechanical force provided by ball milling method is a simplified and effective way to create the defects of the commercial V_2O_5 itself, which is resulted from the release of oxygen from the crystal lattice. Oxygen vacancies were induced by direct mechanical ball milling using commercial V_2O_5 powders. The electrochemical investigation and the migration energy calculation through density functional theory (DFT) for pure V_2O_5 and O_v–V_2O_5 implies that oxygen vacancies can obviously enhance the diffusion of Zn ions, which significantly strengthen the capability of Zn ions storage for commercial V_2O_5 powders. O_v–V_2O_5 show much higher capacity of 410.2 mAh g^{-1} than the pristine commercial V_2O_5(286.9 mAh g^{-1}). Thus, the O_v–V_2O_5 fabricated by facile mechanical ball milling method is promising for future application of low cost and large-scale cathodic materials in AZIBs.

Results and Discussion

Synthesis and characterization of O_v–V_2O_5

O_v–V_2O_5 was fabricated through mechanical ball milling method as shown in Figure 1(a). The ball milling method can provide abundant mechanical force for particles, such as compression and shear forces. Since crystal can produce defects by physical force, here, oxygen vacancies were naturally induced by the strong mechanical force. The oxygen vacancies
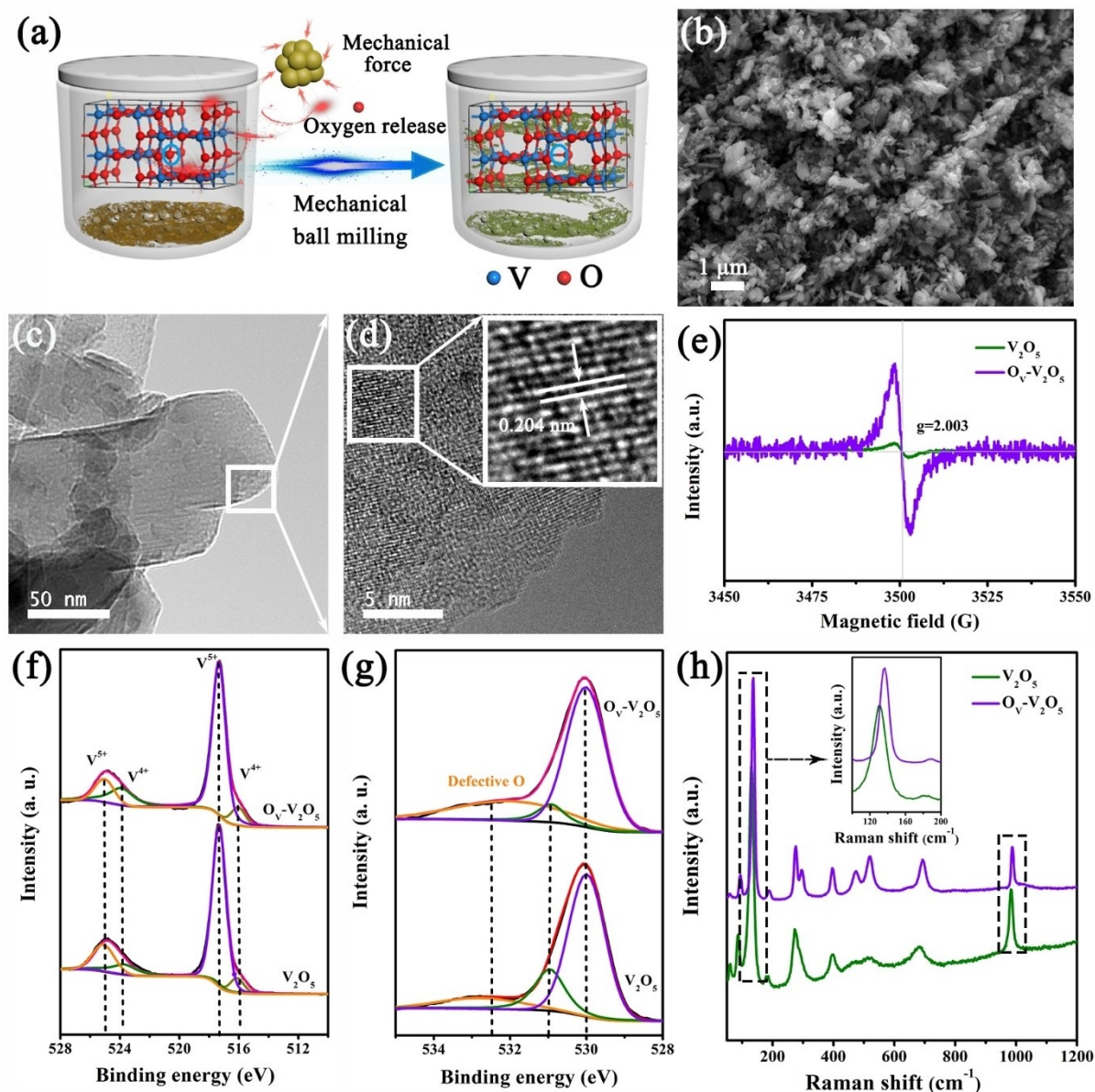

Figure 1. a) Schematic of the methodology to fabricate the O_v–V_2O_5. b) SEM image of the O_v–V_2O_5 powders. c and d) TEM and HRTEM images of O_v–V_2O_5. e) EPR spectra of commercial V_2O_5 and O_v–V_2O_5. f and g) V and O XPS spectra of commercial V_2O_5 and O_v–V_2O_5. h) Raman spectra of commercial V_2O_5 and O_v–V_2O_5.

Batteries & Supercaps

Research Article
doi.org/10.1002/batt.202100341

Chemistry Europe
European Chemical
Societies Publishing

are resulted from the crystal lattice destruction and the release of oxygen in the commercial V_2O_5 powders. The color of the commercial V_2O_5 powder changes from yellow to yellowish green after introducing with mechanical ball milling process (Figure S1a in Supporting Information), indicating the presence of oxygen defects for that low valent V-based oxides show darker color. The scanning electron microscopy (SEM) image of the O_v–V_2O_5 show ordinary particles with the size distribution of 50–300 nm (Figure 1b). The morphology and size of the O_v–V_2O_5 particles have non-essential difference comparing with the commercial V_2O_5 particles (Figure S1b in supporting information). Additionally, the X-ray diffraction (XRD) results of the O_v–V_2O_5 in Figure S2 exhibit nearly the same patterns with commercial V_2O_5 (JCPDS: 41-1426). Transmission electron microscopy (TEM) image was performed as shown in Figure 1(c), the related high resolution transmission electron microscopy (HRTEM) in Figure 1(d) displays an interplanar space of 0.204 nm, corresponding to the (202) plane of orthorhombic V_2O_5. Pentavalent V ion is electron paramagnetic resonance (EPR) silent because of the integer spin, thus the high EPR intensity of the O_v–V_2O_5 (Figure 1e) demonstrate the oxygen defect state in commercial V_2O_5 after inflicted with mechanical force. X-ray photoelectron spectroscopy (XPS) was further performed to highlight the oxygen-deficient structure of O_v–V_2O_5. Firstly, the $V2p_{1/2}$ and $V2p_{3/2}$ spectra were proceeded as shown in Figure 1(f). It is found that the corresponding V^{4+} peaks of O_v–V_2O_5 located at 523.9 and 515.8 eV were obviously strengthened comparing with that for commercial V_2O_5, indicating that V^{5+} was reduced to be V^{4+} after performing with mechanical force.[13] The O 1s spectra are deconvoluted into lattice oxygen (V–O) at 530.1 eV and hydroxyl groups (V–O–H) of defective oxygen at 532.4 eV (Figure 1g).[11,14] The increased intensity in defective oxygen of O_v–V_2O_5 based on the fitting areas indicates the successful introduction of oxygen vacancies. Figure 1(h) shows the Raman spectra of the commercial V_2O_5 and O_v–V_2O_5. The Raman peaks at 131.3 (either B_{1g} or B_{3g}; B_{1g}/B_{3g}), 182.4 (A_g/B_{2g}), 272.8 (B_{1g}/B_{3g}), 290.7 (A_g), 397.9 (A_g), 473.9 (A_g), 510.7 (A_g), 679 (B_{1g}/B_{3g}) and 982.8 (A_g) cm^{-1} confirm the presence of V_2O_5 phase.[15] The peak located at 131.3 cm^{-1} shifts to a higher wavenumber of 136.8 cm^{-1}, which exemplify the decrease of V valence in O_v–V_2O_5 due to the generation of the oxygen vacancies. The energy dispersive X-ray spectroscopy (EDS) test in Figure S3(a) ensures that the atom ratio of oxygen is 70.78% in commercial V_2O_5, which is very close to the ideal V_2O_5 crystal. However, the atom ratio decreases to 63.84% after the mechanical ball milling process (Figure S3b), exactly implying the oxygen deficient of O_v–V_2O_5. Till now, the EPR, XPS, Raman and EDS results all indicate that the mechanical force induced the generation of oxygen vacancies.

Electrochemical performance

Galvanostatic charge-discharge (GCD) curves of commercial V_2O_5 and O_v–V_2O_5 were compared as shown in Figure 2(a). The discharge capacity of O_v–V_2O_5 at the current density of 0.1 A g^{-1}

reached 410.2 mAh g^{-1}, much higher the commercial V_2O_5 (286.9 mAh g^{-1}), implying that the oxygen vacancies involved V_2O_5 expresses much higher capacity than the pure commercial V_2O_5. It should be noticed that the charge/discharge voltage platforms of O_v–V_2O_5 are lower and higher than the commercial V_2O_5, respectively, suggesting that the charge/discharge energy barrier with oxygen vacancies is lower than the pristine V_2O_5. The cyclic voltammetry (CV) curves in Figure 2(b) also imply the superior electrochemical performance of O_v–V_2O_5, for that the peaks belonging to the O_v–V_2O_5 is much stronger and prominent than the commercial V_2O_5. The potentials for the oxidation (0.81 and 1.14 V) and reduction (0.53 and 0.85 V) peaks of O_v–V_2O_5 are respectively lower and higher than that for commercial V_2O_5, which is consistent with the verdict in GCD curves, again proving the lower migration energy barrier of Zn ions in O_v–V_2O_5. The CV curves of O_v–V_2O_5 with various scan rates are shown in Figure S4. The CV shape kept well until the scan rate reaches to 20 mV s^{-1}, reflecting its fast electrochemical reaction and high charge/discharge rate. To further investigate the electrochemical kinetic processes of commercial V_2O_5 and O_v–V_2O_5, CV curves with various scan rates from 0.1 to 2 mV were investigated as shown in Figure S5(a and d), *"b"* value (Figure S5b and e) and the ratio of diffusion-controlled/capacitive contribution (Figure S5c and f) were evaluated.[16] As the sweep rate increases, the entire battery is more affected by the capacitive control both for V_2O_5 and O_v–V_2O_5. The ratio of capacitive capacity is stably increased with the scan rates from 0.1 to 2 mV. However, the diffusion control and capacitive capacity for commercial V_2O_5 is very unstable at different scan rates, indicating its uneven diffusion of Zn ions in commercial V_2O_5 crystal lattice. To further unravel the kinetics of Zn^{2+} transfer at the interface of cathode/electrolyte, electrochemical impedance spectroscopy (EIS) was performed using O_v–V_2O_5 and commercial V_2O_5 as the cathodes respectively (Figure 2c). The charge transfer resistance of O_v–V_2O_5 is only 8 Ω, but the value reached 41 Ω for commercial V_2O_5, which indicates that oxygen vacancies are beneficial for the charge transfer. The rate performance of O_v–V_2O_5 and commercial V_2O_5 were also investigated as shown in Figure 2(d). It is found that the capacity of O_v–V_2O_5 is superior at the various charge/discharge rates. The capacity of O_v–V_2O_5 still kept at 256 mAh g^{-1} at the current density of 2 A g^{-1}, on the contrast, only 105 mAh g^{-1} for pure V_2O_5. To evaluate the long-term stability of the commercial V_2O_5 and oxygen vacancies involved V_2O_5, the cathodes were endured with 2500 cycles respectively at the current density of 2 A g^{-1} (Figure 2e). The commercial V_2O_5 shows poor stability with the capacity retention of only 62.7% after 2500 cycles and low capacity below 80 mAh g^{-1}. On the contrary, the initial capacity of O_v–V_2O_5 reached 262.5 mAh g^{-1} and it still kept 223.6 mAh g^{-1} even after 2500 cycles. The coulombic efficiency of Ov–V_2O_5 approaches to 100% in all cycles. The capacity and cycle stability of O_v–V_2O_5 were compared with other recent reports in Table S1. The performance is still conspicuous although O_v–V_2O_5 was directly fabricated from commercial ordinary V_2O_5 particles without any complex processes and high-cost raw materials.
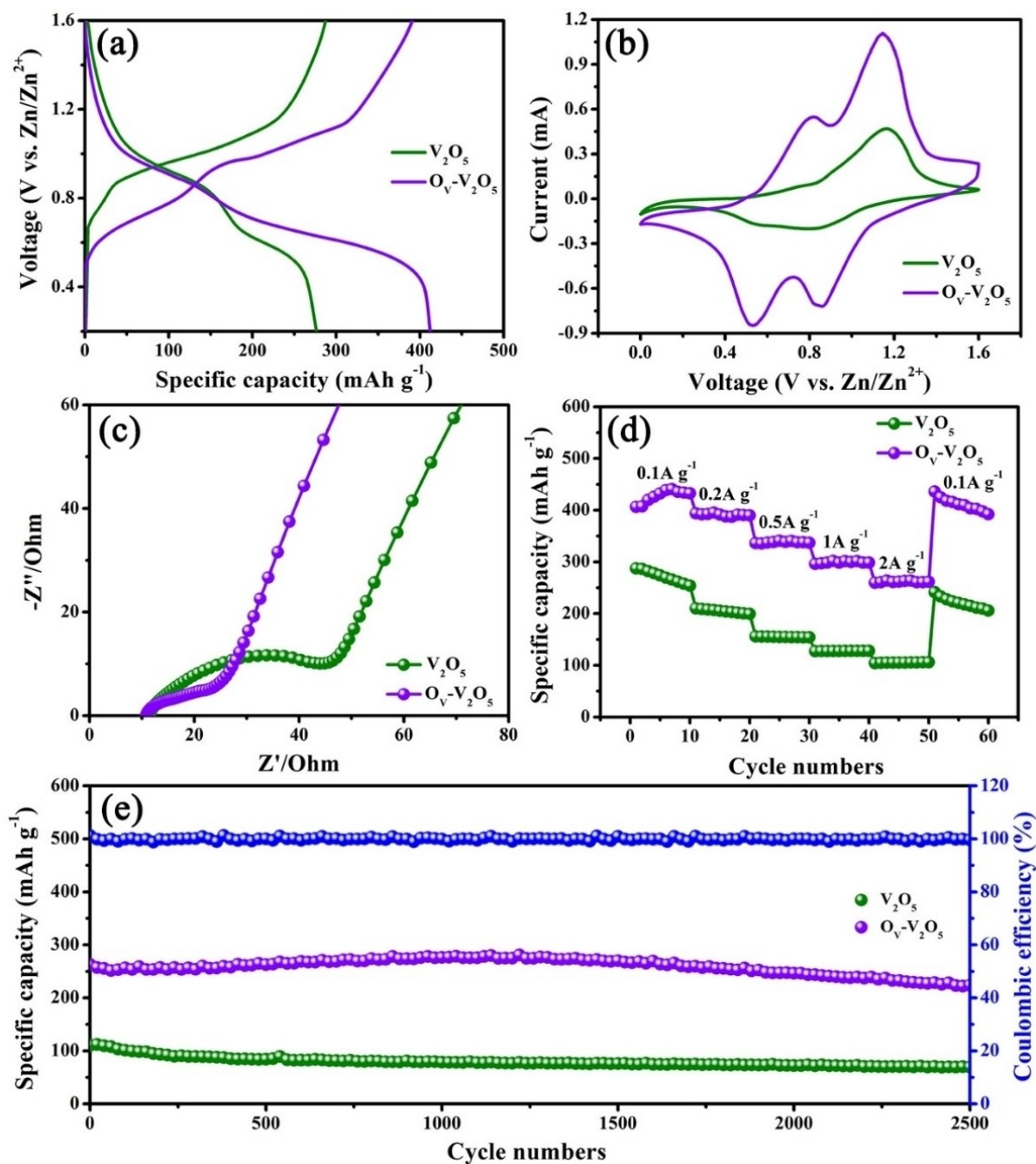
Figure 2. a) Galvanostatic charge-discharge curves of commercial V_2O_5 and O_v–V_2O_5 at a current density of 0.1 A g^{-1}. b) CV curves of commercial V_2O_5 and O_v–V_2O_5 at a sweep rate of 0.5 mV s^{-1}. c) Electrochemical impedance spectra of commercial V_2O_5 and O_v–V_2O_5. d) Rate performance of the commercial V_2O_5 and O_v–V_2O_5. e) Cyclic stability test of commercial V_2O_5 and O_v–V_2O_5 at a current density of 2 A g^{-1}.

Investigation for the insertion of Zn ions in O_v–V_2O_5

XRD patterns (Figure 3b) at different charge/discharge states were characterized according to the various charge/discharge voltage platforms (Figure 3a), the corresponding current density is 0.1 A g^{-1}. It is found that a new peak located at 10.60° appears when the battery was discharged over the first plantform (point B), corresponding to the interlayer distances of 8.83 Å. In addition to the enhanced intensity of the above new peak, another new peak located at 26.59° is followed to

appear with the interlayer distances of 3.55 Å after fully discharge (Point C). The XRD resutls reflect that the lattice space of O_v–V_2O_5 expands at the initial discharge stage resulted from the insertion of Zn ions, then a new phase formed after further more Zn^{2+} insertion. In charge processes, the phase change is fully reversible for that the new peak at 26.59° disappears when undergo the first voltage platform (point D) and then the peak with lower degree at 10.60° also vanishes after fully charge (point E). The XPS spectra of V2p$_{1/2}$ and V2p$_{3/2}$ were detected to investigate the valence change of V before
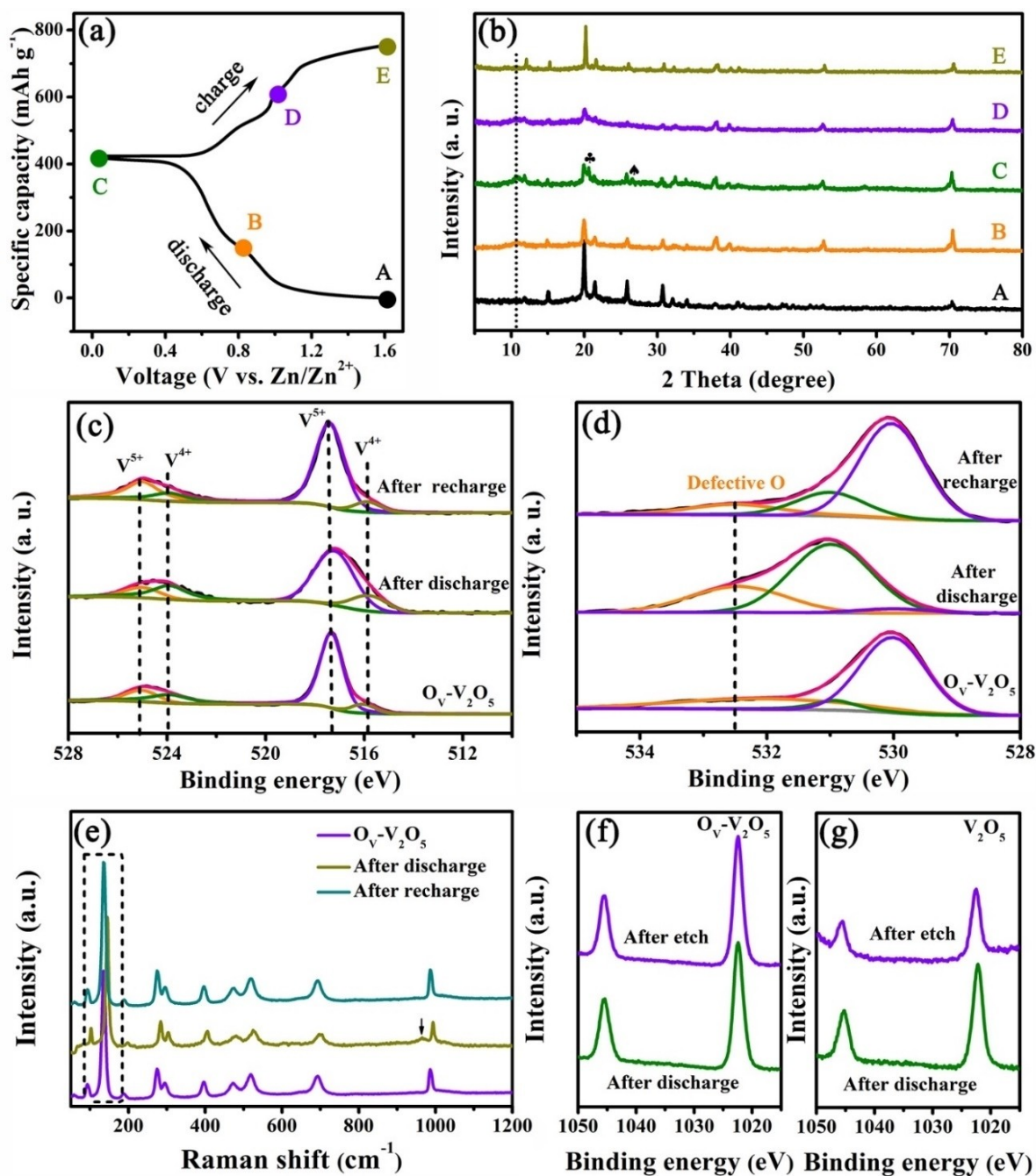
Batteries & Supercaps

Research Article
doi.org/10.1002/batt.202100341

Chemistry Europe
European Chemical
Societies Publishing

Figure 3. a) Charge/discharge curves of O_v–V_2O_5 at the current density of 0.1 A g^{-1}, which is divided into five stages of A–E according to the various voltage platforms. b) XRD patterns at different charge/discharge stages. c and d) V and O XPS spectra of pristine, discharged (insertion with Zn^{2+}) and recharged (extraction of Zn^{2+}) O_v–V_2O_5. e) The Raman spectra for pristine, discharged and recharged O_v–V_2O_5. f and g) Zn XPS spectra of discharged V_2O_5 and O_v–V_2O_5 before and after etch.

and after Zn^{2+} insertion as shown in Figure 3(c). It is found that V^{5+} is further reduced to V^{4+} due to the insertion of Zn ions. O 1s spectra in Figure 3(d) confirm that defective oxygen is drastically strengthened with Zn^{2+} insertion, demonstrating that O_v–V_2O_5 show huge phase change and more oxygen defect after discharge. Those peaks recover to their pristine states again after recharged, indicating the high reversibility of the O_v–V_2O_5-Zn battery. As shown in Figure 3(e), the wavenumbers of Raman spectra show positive shift after discharge,

specially, the peak located at 136.8 cm^{-1} shifts to a higher wavenumber of 144.9 cm^{-1}, reflecting that the V–O bonds are obviously influenced due to the insertion of Zn ions.[15a,b,d,17] Additionally, a new peak at 965.8 cm^{-1} appears after discharge, which directly implies the insertion of Zn ions and the formation of $Zn_xV_2O_5$ compound. Similar as the results in XPS characterizations, O_v–V_2O_5 show superior Zn^{2+} insertion and extraction ability since the Raman spectra also revert to their pristine patterns after recharge. The SEM-EDS mapping images

of elements V, O and Zn in Figure S6 strongly confirm that Zn is uniformly distributed in O_v–V_2O_5 after charge.

Zn 2p XPS spectra was performed to investigate the surface and internal information after Zn^{2+} insertion. The peaks of Zn 2p spectra (Figure 3f) nearly remain unchanged after etching by ion bombardment for 400 s, which indicates that Zn ions inserted deeply into the internal lattice of O_v–V_2O_5.[6b,7a] However, the peaks intensity of Zn 2p spectra in Figure 3(g) obviously decreased with the same etching time for commercial V_2O_5, proving that Zn ions mainly exist on the surface of commercial V_2O_5 and those ions show clumsy electrochemical kinetics and poor diffusion capability. Thus, O_v–V_2O_5 show more facile process for Zn ions diffusion. The EDS data in Figure S7 directly demonstrate the higher energy storage capacity of O_v–V_2O_5, for that the atomic ratio of Zn/V in discharged O_v–V_2O_5 is 1.52, but the value in commercial V_2O_5 is only 0.86. This conclusion is again ensured by XPS characterization as shown in Figure S8 in supporting information, the atomic ratio of Zn/V tested by XPS after discharge is 1.58 and 0.79 for O_v–V_2O_5 and commercial V_2O_5 respectively. The Zn content of O_v–V_2O_5 in EDS and XPS spectra is nearly doubled comparing with that for commercial V_2O_5, which is exactly in agreement with the capacity test results shown in Figure 2(a). The XPS and EDS results prove that the amount of inserted Zn^{2+} in O_v–V_2O_5 is higher than the commercial V_2O_5 after discharge, which is resulted from the lower diffusion energy barriers of O_v–V_2O_5.

To further verify the conclusion that high capacity is resulted from the oxygen vacancies, we refund the oxygen of O_v–V_2O_5 through calcination in air at a lower temperature of 300 °C. The calcination process with low temperature keeps the morphology unchanged (Figure S9) to avoid the influence of morphology in performance research. As shown in Figure S10, the peaks of O_v–V_2O_5 in Raman spectra after calcination return to a lower wavenumber, nearly the same as the previous commercial V_2O_5, illustrating that oxygen is returned after calcination. The EDS results exhibit the oxygen content of 70.83% after calcination (Figure S11), very close to the commercial V_2O_5 with the value of 70.78%, which directly confirm that the V_2O_5 particles with none-oxygen vacancies are fabricated through the calcination of O_v–V_2O_5 in low temperature. Then, the performance of this oxygen vacancies free V_2O_5 electrode was investigated to compare with the O_v–V_2O_5 cathode as shown in Figure S11. The capacity and rate performance are sharply decreased as shown in Figures S12(a, b). The electrode without oxygen vacancies show higher charge transfer resistance than that for previous O_v–V_2O_5 (Figures S12c), indicating that oxygen vacancies are the key to reduce the energy barrier of charge transfer. The long charge/discharge cyclic performance in Figure S12(d) shows poor capacity and cycle stablity, which illustrates the high capacity and long cycle life are originated from the oxygen vacancies. H_2 annealing is also one of the most common method to fabricate the oxygen vacancies. Here, we also fabricated the commercial V_2O_5 powders with oxygen vacancies by annealing in H_2 (H_2–V_2O_5) and investigated their performance (Figure S13 and S14). Under the annealing temperature of 400 °C, the materials show

uneven color with black color at the top and yellow at the bottom (Figure S13a), which indicates that the oxygen vacancies are not uniform. To verify the oxygen vacancies distribution in the porcelain boat, EDS was performed to investigate the oxygen content of the V_2O_5 at the top and bottom positions respectively as shown in Figure S13(b and c). The results show that the oxygen content at the top position is only about 60%. However, the value at the bottom position is 69.6%, which is very close to the pure commercial V_2O_5 (70.8% in Figure S3a). XRD patterns in Figure S13d also indicates that the oxygen vacancies are not uniform due to their two phases of V_2O_5 and V_6O_{13}. The uneven oxygen content was resulted from the low weight of H_2, H_2 is hard to infiltrate in the bottom sample if the material is spread thicker (Figure S13e). Additionally, comparing with the ball milling method (Figure 1b), the high temperature resulted the agglomeration of the commercial V_2O_5 particles as shown in Figure S14(a). Thus, the H_2–V_2O_5 show slightly lower capacity and rate performance comparing with the O_v–V_2O_5 in Figure S14(b and c). In summary, H_2 annealing is not an appropriate method to fabricate the oxygen vacancies of commercial V_2O_5 in future large-scale materials fabrication.

Migration mechanism research

To systematically investigate the greatly enhanced Zn^{2+} storage performance, the diffusion coefficient of Zn^{2+} (D_{Zn}) in O_v–V_2O_5 was identified by the galvanostatic intermittent titration technique (GITT, Figure 4a, b). The average D_{Zn} values of O_v–V_2O_5 at the charge and discharge plateaus were about 6.17×10^{-14} and 2.08×10^{-14} $cm^2 S^{-1}$, respectively. In contrast, the electrode exhibited an obviously lower D_{Zn} (2.27×10^{-15} and 6.15×10^{-15}), indicating the sluggish mobility during Zn^{2+} storage/release. The GITT results indicate the high-efficiency diffusion ability of Zn ions in O_v–V_2O_5 crystal. To understand the migration mechanism of Zn^{2+} in O_v–V_2O_5 and pure V_2O_5, density functional theory (DFT) calculations were performed to analyze the relative energy for the migration of Zn^{2+} as shown in Figures 4c and 4d. Zn ions move along the direction of a axis and the migration pathways are between sites in the order of $Zn_1 \rightarrow Zn_2 \rightarrow Zn_1$. Notably, the energy barrier of O_v–V_2O_5 is obviously lower than the pure V_2O_5 without oxygen vacancies, indicating that the oxygen vacancies of commercial V_2O_5 induced by mechanical force are effective to enhance the diffusion of Zn ions..

Conclusion

Oxygen vacancies involved commercial V_2O_5 cathode is fabricated through a simple mechanical ball milling method. It is found that mechanical force can directly induce the oxygen vacancies in commercial V_2O_5. The capacity of the O_v–V_2O_5 is obviously optimized comparing with the pristine commercial V_2O_5. The high performance of O_v–V_2O_5 is resulted from the low diffusion energy barrier of Zn ions, which is confirmed by both
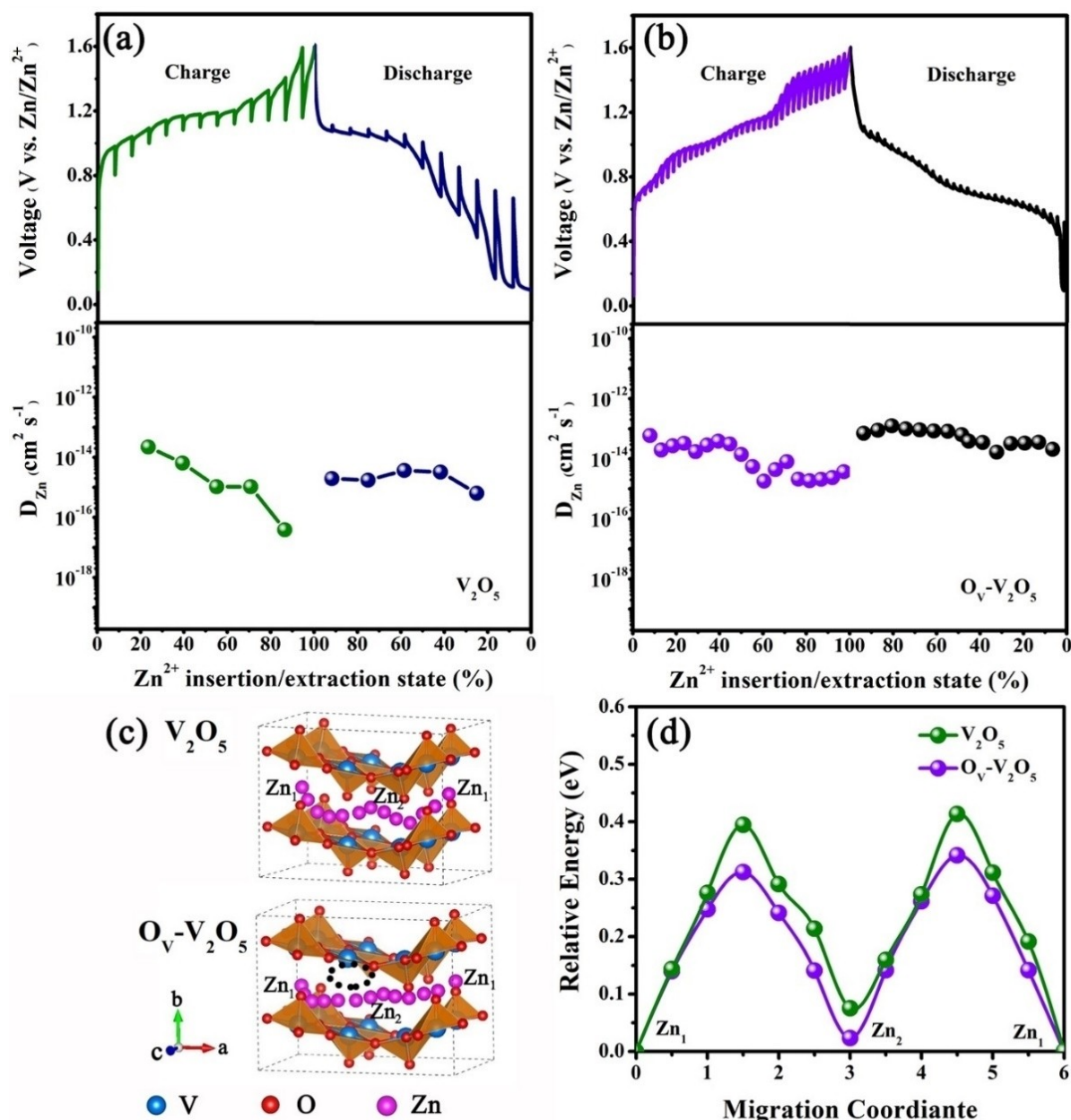
Figure 4. a and b) GITT profiles and calculated Zn^{2+} diffusion coefficient of V_2O_5 and O_v–V_2O_5 electrodes. c and d) The DFT calculation of the relative energy and the corresponding pathways for Zn-ion migration.

electrochemical investigation and DFT calculation in theory. The facile synthesis technology is promising for future high-performance, low-cost, safe, and environment-friendly commercial Zn battery devices application.

Experimental Section

Materials

Preparation of O_v–V_2O_5: O_v–V_2O_5 nanoparticles were synthesized through a simple mechanical ball milling method. 4 g of commercial V_2O_5 powders was added into ball grinding tanks (2 g in each tank to keep the equilibrium). Then, the sample was

mechanically ball-milled for 4 h to obtain the oxygen vacancies containing commercial V_2O_5 powders. Additionally, the prepared O_v–V_2O_5 was calcined at 300 °C for 2 h in O_2 to dislodge the oxygen vacancies in O_v–V_2O_5.

Characterizations

The morphology and microstructure of the prepared samples were characterized using feld-emission scanning electron microscopy (SEM, JEOLJSM-7900F) and transmission electron microscopy (TEM, Titan G260-300 with a probe corrector). X-ray diffraction (XRD, PANalytical X'PertPRO) and Raman spectrometry (LabRAM HR JYEvolution, 532 nm) were carried out to observe the chemical composition of the prepared samples. The elements content and distribution were detected by Energy dispersive X-ray spectroscopy

Batteries & Supercaps

Research Article
doi.org/10.1002/batt.202100341

Chemistry Europe
European Chemical
Societies Publishing

(EDS, JEOLJSM-7900F). Besides the Raman spectra and EDS data, the presence of oxygen vacancies in O_V–V_2O_5 was also investigated by X-ray photoelectron spectroscopy (XPS, EscaLab 250Xi) and electron paramagnetic resonance (EPR, Bruker A300).

Electrochemical measurements

All the electrochemical measurements were conducted by employing an electrochemical workstation (CHI760E) and battery testing system (NEWARE, A211-BTS-4S-1U). The full battery was assembled by CR2032 coin cell, in which Zn foil, glass fiber membrane and 2 M $ZnSO_4$ solution were served as the anode, separator and electrolyte respectively. The galvanostatic intermittent titration technique (GITT) was employed to investigate the diffusion situation of Zn ions. With GITT curves, the following equation was introduced to calculate the solid diffusion coefficient:

where τ is the relaxation time (s). n_m, V_m and S represented the number of moles (mol), the molar volume of the electrode material (cm^3) and the electrode/electrolyte contact are (cm^2). ΔE_s is the voltage change caused by the current pulse. ΔE_t is the voltage change of constant current charge-discharge.

Computational methods

We have employed the Vienna Ab Initio Package (VASP)[18] to perform all the density functional theory (DFT) calculations within the generalized gradient approximation (GGA) using the PBE[19] formulation. We have chosen the projected augmented wave (PAW) potentials to describe the ionic cores and take valence electrons into account using a plane wave basis set with a kinetic energy cutoff of 450 eV.[20] Partial occupancies of the Kohn-Sham orbitals were allowed using the Gaussian smearing method and a width of 0.05 eV. The electronic energy was considered self-consistent when the energy change was smaller than 10^{-5} eV. A geometry optimization was considered convergent when the force change was smaller than 0.03 eVÅ^{-1}. Grimme's DFT-D3 methodology was used to describe the dispersion interactions.[21]

The equilibrium lattice constants of V_2O_5 unit cell were optimized, when using a $4\times4\times4$ Monkhorst-Pack k-point grid for Brillouin zone sampling. We then use it to construct a supercell model V_2O_5 in the $\times$ and y directions. During structural optimizations, the $3\times3\times3$ Monkhorst-Pack k-point grid for Brillouin zone was used for k-point sampling for surface structure. The climbing-image nudged elastic band methods had been employed to calculation the energy.

Supporting Information

Supporting Information is available from the Wiley Online Library or from the author.

Acknowledgements

Conflict of Interest

The authors declare no conflict of interest.

Data Availability Statement

The data that support the findings of this study are available from the corresponding author upon reasonable request.

[1] a) J. Luo, W. Cui, P. He, Y. Xia, *Nat. Chem.* **2010**, *2*, 760; b) P. Simon, Y. Gogotsi, B. Dunn, *Science* **2014**, *343*, 1210; c) Q. Zhu, D. Zhao, M. Cheng, J. Zhou, K. A. Owusu, L. Mai, Y. Yu, *Adv. Energy Mater.* **2019**, *9*, 1901081; d) Q. Zhu, M. Cheng, B. Zhang, K. Jin, S. Chen, Z. Ren, Y. Yu, *Adv. Funct. Mater.* **2019**, *29*, 1905979.

[2] a) J. Parker, C. Chervin, I. Pala, M. Machler, M. Burz, J. Long, D. Rolison, *Science* **2017**, *356*, 415; b) H. Pan, Y. Shao, P. Yan, Y. Cheng, K. S. Han, Z. Nie, C. Wang, J. Yang, X. Li, P. Bhattacharya, K. T. Mueller, J. Liu, *Nat. Energy* **2016**, *1*, 16039; c) D. Chao, C. Zhu, M. Song, P. Liang, X. Zhang, N. Tiep, H. Zhao, J. Wang, R. Wang, H. Zhang, H. Fan, *Adv. Mater.* **2018**, *30*, 1803181.

[3] a) J. Goodenough, K.-S. Park, *J. Am. Chem. Soc.* **2013**, *135*, 1167; b) L. Wang, K.-W. Huang, J. Chen, J. Zheng, *Sci. Adv.* **2019**, *5*, eaax4279; c) Q. Zhu, M. Cheng, X. Yang, B. Zhang, Z. Wan, Q. Xiao, Y. Yu, *J. Mater. Chem. A* **2019**, *7*, 6784.

[4] a) Y. Liang, H. Dong, D. Aurbach, Y. Yao, *Nat. Energy* **2020**, *5*, 646; b) D. Chao, W. Zhou, F. Xie, C. Ye, H. Li, M. Jaroniec, S.-Z. Qiao, *Sci. Adv.* **2020**, *6*, eaba4098; c) N. Zhang, X. Chen, M. Yu, Z. Niu, F. Cheng, J. Chen, *Chem. Soc. Rev.* **2020**, *49*, 4203; d) Q. Zhu, L. Yu, S. Song, D. Wang, D. Zhao, J. Zhou, Y. Yu, S. Chen, Z. Ren, *Mater. Today Phys.* **2021**, *19*, 100425.

[5] a) F. Wang, E. Hu, W. Sun, T. Gao, X. Ji, X. Fan, F. Han, X.-Q. Yang, K. Xu, C. Wang, *Energy Environ. Sci.* **2018**, *11*, 3168; b) F. Wan, L. Zhang, X. Dai, X. Wang, Z. Niu, J. Chen, *Nat. Commun.* **2018**, *9*, 1656; c) G. Yadav, J. Gallaway, D. Turney, M. Nyce, J. Huang, X. Wei, S. Banerjee, *Nat. Commun.* **2017**, *8*, 14424.

[6] a) C. Zhong, B. Liu, J. Ding, X. Liu, Y. Zhong, Y. Li, C. Sun, X. Han, Y. Deng, N. Zhao, W. Hu, *Nat. Energy* **2020**, *5*, 440; b) Q. Zhu, Q. Xiao, B. Zhang, Z. Yan, X. Liu, S. Chen, Z. Ren, Y. Yu, *J. Mater. Chem. A* **2020**, *8*, 10761; c) D. Kundu, B. Adams, V. Duffort, S. Vajargah, L. Nazar, *Nat. Energy* **2016**, *1*, 16119; d) Y. Yang, Y. Tang, G. Fang, L. Shan, J. Guo, W. Zhang, C. Wang, L. Wang, J. Zhou, S. Liang, *Energy Environ. Sci.* **2018**, *11*, 3157.

[7] a) D. Kundu, S. Hosseini Vajargah, L. Wan, B. Adams, D. Prendergast, L. F. Nazar, *Energy Environ. Sci.* **2018**, *11*, 881; b) K. Nam, H. Kim, J. Choi, J. Choi, *Energy Environ. Sci.* **2019**, *12*, 1999.

[8] J. Huang, Z. Wang, M. Hou, X. Dong, Y. Liu, Y. Wang, Y. Xia, *Nat. Commun.* **2018**, *9*, 2906.

[9] a) K. Zhu, T. Wu, K. Huang, *Adv. Energy Mater.* **2019**, *9*, 1901968; b) C. Xia, J. Guo, P. Li, X. Zhang, H. Alshareef, *Angew. Chem. Int. Ed.* **2018**, *57*, 3943; c) L. Shan, Y. Yang, W. Zhang, H. Chen, G. Fang, J. Zhou, S. Liang, *Energy Storage Mater.* **2019**, *18*, 10.

[10] a) V. Soundharrajan, B. Sambandam, S. Kim, M. H. Alfaruqi, D. Y. Putro, J. Jo, S. Kim, V. Mathew, Y.-K. Sun, J. Kim, *Nano Lett.* **2018**, *18*, 2402; b) P. Hu, T. Zhu, X. Wang, X. Wei, M. Yan, J. Li, W. Luo, W. Yang, W. Zhang, L. Zhou, Z. Zhou, L. Mai, *Nano Lett.* **2018**, *18*, 1758-.

[11] M. Liao, J. Wang, L. Ye, H. Sun, Y. Wen, C. Wang, X. Sun, B. Wang, H. Peng, *Angew. Chem. Int. Ed.* **2020**, *59*, 2273.

[12] a) R. M. de Carvalho, T. M. Campos, P. M. Faria, L. M. Tavares, *Powder Technol.* **2021**, *392*, 489–502; b) Ö. Genç, A. H. Benzer, *Miner. Eng.* **2015**, *74*, 20–29.

[13] a) D. Zhao, Q. Zhu, D. Chen, X. Li, Y. Yu, X. Huang, *J. Mater. Chem. A* **2018**, *6*, 16475; b) P. Liu, K. Bian, K. Zhu, Y. Xu, Y. Gao, H. Luo, L. Lu, J. Wang, J. Liu, G. Tai, *ACS Appl. Mater. Interfaces* **2017**, *9*, 17002.

[14] a) Y.-L. Ding, Y. Wen, C. Wu, P. Aken, J. Maier, Y. Yu, *Nano Lett.* **2015**, *15*, 1388; b.

Batteries & Supercaps

Research Article
doi.org/10.1002/batt.202100341

Chemistry Europe
European Chemical
Societies Publishing

[15] a) R. Basu, A. Prasad, S. Dhara, A. Das, *J. Phys. Chem. C* **2016**, *120*, 26539; b) R. Baddour-Hadjean, J. Pereira-Ramos, C. Navone, M. Smirnov, *Chem. Mater.* **2008**, *20*, 1916; c) M. Sreedhara, J. Ghatak, B. Bharath, C. Rao, *ACS Appl. Mater. Interfaces* **2017**, *9*, 3178; d) M. Smirnov, E. Roginskii, K. Smirnov, R. Baddour-Hadjean, J.-P. Pereira-Ramos, *Inorg. Chem.* **2018**, *57*, 9190.

[16] a) J. Li, K. McColl, X. Lu, S. Sathasivam, H. Dong, L. Kang, Z. Li, S. Zhao, A. G. Kafizas, R. Wang, D. J. L. Brett, P. R. Shearing, F. Corà, G. He, C. J. Carmalt, I. P. Parkin, *Adv. Energy Mater.* **2020**, *10*, 2070068; b) H. Dong, J. Li, S. Zhao, Y. Jiao, J. Chen, Y. Tan, D. J. L. Brett, G. He, I. P. Parkin, *ACS Appl. Mater. Interfaces* **2021**, *13*, 745–754.

[17] B. Yin, Z. Liu, Y. Wang, X. Ji, Y. Huan, D. Dong, X. Hu, T. Wei, *ACS Appl. Mater. Interfaces* **2020**, *12*, 45961.

[18] a) G. Kresse, J. Furthmüller, *Comput. Mater. Sci.* **1996**, *6*, 15; b) G. Kresse, J. Furthmüller, *Phys. Rev. B* **1996**, *54*, 11169.

[19] J. Perdew, K. Burke, M. Ernzerhof, *Phys. Rev. Lett.* **1996**, *77*, 3865.

[20] a) G. Kresse, D. Joubert, *Phys. Rev. B* **1999**, *59*, 1758; b) P. Blöchl, *Phys. Rev. B* **1994**, *50*, 17953.

[21] S. Grimme, J. Antony, S. Ehrlich, H. Krieg, *J. Chem. Phys.* **2010**, *132*, 154104.